# Limit states for post-earthquake assessment and recovery analysis of ductile concrete components

Eyitayo A Opabola, M.EERI[1] , Saman A Abdullah, M.EERI[2,3], Kenneth J Elwood, M.EERI[4], and John Wallace, M.EERI[2]

## Abstract

Post-earthquake assessment procedures require component deformation limits to identify locations for visual inspection and locations needing structural repair. This study proposes a framework for defining component deformation limits for detailed visual inspection and repair for earthquake-damaged concrete buildings. First, observations from cyclic tests of ductile concrete components (beams, columns, and walls) suggested that the residual capacity (in terms of strength and deformation capacity) of such components is likely uncompromised if the deformation at the initiation of lateral strength loss (LSL) is not exceeded in prior loading histories. The results also revealed that the deformation at the initiation of LSL typically corresponds to the onset of longitudinal bar buckling in ductile components. Furthermore, using experimental data, multipliers are developed as fractions of ASCE/SEI 41 modeling parameters at lateral failure (i.e. *a* or *d*) to predict deformation at initiation of LSL. Subsequently, a probabilistic approach is proposed for defining the component deformation limits, considering uncertainty in both capacity and demand. Component deformation limits for detailed visual inspection are defined such that there is a low probability (adopted as <10%) of exceeding the deformation at the initiation of LSL. The component deformation limit for repair is defined as the median deformation at the initiation of LSL (i.e. 50% probability of exceedance).

[1]Department of Civil, Environmental and Geomatic Engineering, University College London, London, UK
[2]Department of Civil and Environmental Engineering, University of California, Los Angeles, Los Angeles, CA, USA
[3]Department of Civil Engineering, College of Engineering, University of Sulaimani, Sulaimani, Iraq
[4]Department of Civil and Environmental Engineering, The University of Auckland, Auckland, New Zealand

**Corresponding author:**
Eyitayo A Opabola, Department of Civil, Environmental and Geomatic Engineering, University College London, Gower Street, Bloomsbury, London WC1E 6BT, UK.
Email: e.opabola@ucl.ac.uk

## Introduction

Current design codes and standards (e.g. ACI 318-19, 2019) for seismic design of reinforced concrete (RC) structures permit significant structural damage to pre-designated structural components under design level earthquake (EQ) (DE) for non-essential buildings (Risk Category I, II, and III). Under such large events, components of the lateral force-resisting system are expected to undergo flexural yielding and form plastic hinges. A fundamental design strategy to achieve Life Safety performance objectives in non-essential buildings is to ensure certain non-ductile actions (e.g. shear) remain essentially elastic (capacity design) and that the plastic hinge regions of ductile components are detailed such that they can undergo the inelastic seismic demands without significant strength degradation.

Recent EQs (e.g. 2010 Maule in Chile and 2011 Christchurch in New Zealand) have demonstrated that these modern seismic design principles can generally satisfy Life Safety (LS) performance objectives. However, societal expectations have recently shifted from LS to Functional Recovery performance objectives. This paradigm shift has been catalyzed by the economic losses associated with the widespread closure and demolition of EQ-damaged, code-compliant concrete buildings in recent EQs. For example, many of the multistory buildings demolished after the 2011 Christchurch and 2016 Kaikoura EQs were designed following modern building codes and standards. However, there is some debate as to whether some of these buildings needed to be demolished, that is, repair was a viable option (Marquis et al., 2017). Therefore, following a damaging EQ, the ability to evaluate whether the residual (reserve) capacity of a damaged building satisfies a desired performance objective in a future event is of paramount importance. If it is determined that the desired post-EQ performance objective cannot be satisfied, the building may need to be repaired to restore its structural characteristics. If the repair is not sufficient or viable, then retrofit or demolition are options. This article does not address the topic of retrofit of damaged buildings.

The assessment of the post-EQ residual capacity and repair of buildings has recently gained significant attention globally due to the lack of comprehensive and efficient guidelines. For example, in the United States, the state-of-practice documents for evaluation of EQ-damaged buildings are Federal Emergency Management Agency (FEMA) 306 and 307 (FEMA, 1998a, 1998b), which only include guidance for masonry and concrete wall buildings. Furthermore, various studies (e.g. Moscoso et al., 2021) have highlighted the limitations of these documents for assessing the residual capacity of concrete walls. These limitations are primarily attributed to the lack of experimental data when these documents were developed in the late 1990s. However, there has been a significant increase in the number of component test programs reported in the literature in the last two decades, which can be used to develop more comprehensive guidelines that could inhibit the economic burdens associated with unwarranted long-term closure or demolition of buildings as observed in Christchurch following the 2011 EQ.
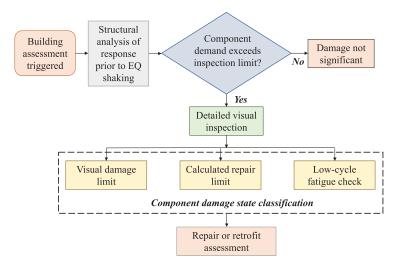
**Figure 1.** Post-earthquake assessment framework under development in the ATC-145 project.

The data from those component test programs are being leveraged by the ongoing Applied Technology Council (ATC)-145 project, *Guide for Repair of Earthquake Damaged Buildings to Achieve Future Resilience*, which is funded the FEMA and managed by the ATC. Figure 1 outlines a post-EQ assessment framework for EQ-damaged buildings under development for the ATC-145. As shown in Figure 1, an analytical model of the damaged building subjected to ground motions recorded at or near the site is used to identify if component demands exceed a detailed visual inspection limit. In this study, the detailed visual inspection limit is defined to correspond to a post-EQ state beyond which some degree of component structural damage is expected, and an immediate damage inspection is required to certify that the building is safe for occupancy. For components requiring detailed visual inspection, component damage classification is carried out using a combination of visual damage inspection, calculated repair limit, and a low-cycle fatigue check. Component damage class can either be no damage, no safety-critical damage, or safety-critical damage. The visual damage inspection entails classifying the observed damage into the component damage class using a database of photos from experimental test programs. Visual damage inspection is outside the scope of this article. The repair limit is defined to correspond to post-EQ state beyond which safety repairs of damaged components are needed in order to restore the strength and deformation capacity of the components. The low-cycle fatigue check is used to determine whether the capacity of the longitudinal reinforcement is materially compromised. For the sake of brevity, further discussions on low-cycle fatigue check of reinforcement are not provided herein; however, interested readers are referred to Elwood et al. (2021), where information on this check is provided.

To aid the development of a post-EQ assessment framework, this study proposes a framework for defining component deformation limits for detailed visual inspection and structural repair of damaged components. As the first step, test data are reviewed to understand the impact of displacement history on the residual capacity of concrete components and to define component deformation limits beyond which: (a) the number of loading cycles begins to influence the strength and deformation capacity of the component and (b) the prior loading history begins to influence the residual capacity (in terms of strength and deformation capacity) of the component for subsequent loading events. This component

deformation limit was found to correspond to the initiation of lateral strength loss (LSL). Subsequently, using test data from ductile concrete beams, columns, and walls, a probabilistic methodology was developed to define component deformation limits for detailed visual inspection and repair. For convenience and practical purposes, these limits are provided as fractions of modeling parameters contained in ASCE/SEI 41, rather than developing new models. Finally, although the applicability of the proposed framework is demonstrated for ductile beams, columns, and walls, the methodology could be applied to other concrete components and components of other materials (e.g. steel components). Such components are, however, outside the scope of this study.

## Impact of loading history on component residual capacity

### Influence of prior number of cycles

For post-EQ residual capacity assessment, it is important to understand the effect of the cyclic loading history imposed on concrete components on the performance of these components in future EQ events. This section reviews experimental results from nominally identical components tested under a varying number of cycles at each peak deformation/load demand to evaluate the effect of loading history.

Kawashima and Koyama (1988) tested three nominally identical, flexure-controlled columns with an aspect ratio of 5.4 subjected to different numbers of cycles at each drift demand to assess the influence of the number of cycles on damage progression and hysteretic response of RC columns. Figure 2 shows the damage accumulation history for two nominally identical columns subjected to 3 and 10 repeated cycles at each drift demand. This figure indicates that the influence of the number of cycles per drift level ($N_{cyc}$) on the component damage level only became significant when the drift demand exceeded 2.1% (corresponding to a ductility demand of 4). Prior to reaching this ductility demand, the damage progression of both specimens was similar irrespective of the number of repeated cycles at each drift level. As indicated in Figure 2 with the red dashed line, this 2.1% drift demand corresponds to the initiation of LSL. As shown in Figure 2, the adopted definition of the point of initiation of LSL throughout this article is the point beyond which a lower peak strength corresponds to the subsequent larger peak deformation demand. It is should be noted that this point is different from the 20% LSL typically adopted in defining the ultimate deformation capacity of components. Similar conclusions were reached when examining the results from another set of tests reported by the same authors on flexure-controlled columns with an aspect ratio of 3.8 (with similar transverse reinforcement detailing as the specimens with an aspect ratio of 5.4).

Similar results have also been observed for RC structural walls. For example, Oesterle et al., (1979) tested two identical flexure-shear-controlled walls with barbell-shaped cross-sections under two different reversed cyclic loading protocols to investigate the significance of loading history on the behavior of the walls, as shown in Figure 3. As can be noted, one reversed cycle at a rotational ductility of five (i.e. roughly drift at the initiation of LSL) resulted in response of Wall B9 being comparable to that of Wall B7, which had sustained three complete reversed cycles at ductility demands of 1 to 5. Thus, the authors concluded that structural wall behavior under load reversals was not dependent on the entire previous load history but instead was dependent on whether the wall was previously loaded to initiation of LSL or not.

These limited experimental results suggest that the number of cycles applied prior to the initiation of LSL may not have a significant influence on the damage progression and
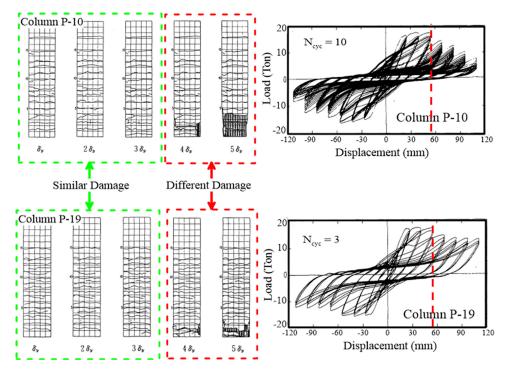
**Figure 2.** Influence of number of repeated cycles on damage progression history and hysteretic response of nominally identical flexure-dominated columns.
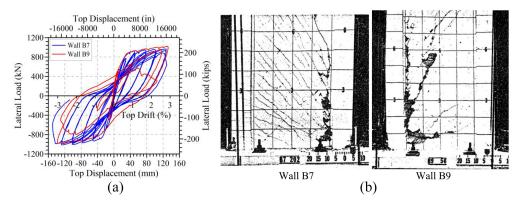*Source.* Kawashima and Koyama (1988).



**Figure 3.** Companion walls tested under different load protocols (Oesterle et al., 1979). (a) load-displacement relation and (b) damage condition at end of test.

hysteretic response of a concrete component, provided that low-cycle fatigue limit state is not triggered.

## Influence of prior maximum deformation demands

Experimental results (Chiu et al., 2021; Colmenares and Santa María, 2021; Maeda et al., 2017; Marder, 2018; Moscoso et al., 2021; Opabola and Elwood, 2023) are reviewed to
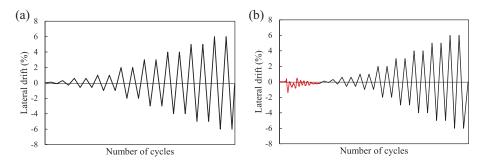
**Figure 4.** Typical loading protocol used to study the residual capacity of concrete components:
(a) standard cyclic loading protocol (b) standard cyclic loading protocol preceded by a prior loading
protocol or ground motion.

understand the limit state at which demands from a past seismic event have compromised
the residual capacity of a component in future seismic events. Each test program includes
two or more tests on nominally identical components—one of which is subjected to a standard cyclic loading protocol (Figure 4a), and the other specimen(s) subjected to an initial
loading protocol (an EQ or a cyclic loading) prior to applying a standard cyclic loading
protocol (Figure 4b).

First, six nominally-identical ductile beam specimens reported by Marder et al. (2018)
were examined. The test specimens included: (1) Specimen CYC subjected to a quasi-static
standard cyclic protocol; (2) Specimen CYC-DYN subjected to a pseudo-dynamic standard cyclic protocol; (3) Specimen LD-1 subjected to an initial pseudo-dynamic long-duration displacement history (with a peak drift demand of 1.36%) is applied and followed by
a quasi-static standard cyclic protocol; (4) Specimen LD-2 subjected to an initial pseudo-
dynamic long-duration displacement history (with a peak drift demand of 2.17%) followed by a quasi-static standard cyclic protocol; (5) Specimen P-1 subjected to an initial
pseudo-dynamic pulse-type displacement history (with a peak drift demand of 1.36%) followed by a quasi-static standard cyclic protocol; (6) Specimen P-2 subjected to an initial
pseudo-dynamic pulse-type displacement history (with a peak drift demand of 2.17%) followed by a quasi-static standard cyclic protocol. The measured drift at the initiation of
LSL for specimen CYC-DYN was 1.9%, which means that specimens LD-1 and P-1 were
subjected to an initial pseudo-dynamic loading protocol with a peak drift (1.36%) smaller
than the drift at the initiation of LSL from a nominally identical specimen subjected to a
standard cyclic protocol. On the other hand, specimens LD-2 and P-2 were subjected to
initial dynamic loading protocols with a peak drift (2.17%) larger than the drift at the
initiation of LSL from a nominally identical specimen subjected to a standard cyclic protocol. A summary of the test results is presented in Table 1. The force–displacement plots
of the beam specimens are presented in Figure 5. It is noted that Figure 5 presents only
the hysteretic behavior during the standard cyclic loading protocol of specimens LD-1,
LD-2, P-1, and P-2. The tests showed that the initial EQ protocol influenced the initial
stiffness of the damaged specimens (the residual displacements in the EQ-damaged specimens are also noteworthy—see Figure 5e). This article focuses on the influence of initial
EQ protocol on residual strength and deformation capacity of components. Studies on the
influence of initial EQ protocol on the initial stiffness of the EQ-damaged frame components are available in existing literature (Abdullah et al., 2020; Di Ludovico et al., 2013;
Marder, 2018; Opabola and Elwood, 2023).

**Table 1.** Summary of the Marder et al. (2018) tests on nominally identical ductile beam specimens

| Specimen | Loading protocol | Peak drift demand from initial earthquake loading history (%) | Measured ultimate deformation capacity at $0.8V_{max}$ |
|---|---|---|---|
| LD-1 | EQ + Standard[*] | 1.36 | 4.3 |
| LD-2 | EQ + Standard[*] | 2.17 | 3.3 |
| P-1 | EQ + Standard[**] | 1.36 | 4.9 |
| P-2 | EQ + Standard[**] | 2.17 | 3.3 |

LD: long-duration; P: Pulse-type; EQ: earthquake.

The baseline nominally identical specimen subjected to a standard dynamic cyclic loading protocol (specimen CYC-DYN) had a measured drift at initiation of lateral strength loss of 1.9%. The baseline nominally identical specimen subjected to a standard quasi-static cyclic loading protocol (specimen CYC) had a measured drift at 20% drop in lateral resistance ($0.8V_{max}$) of 4.3%.

[*]Specimen subjected to an initial dynamic long-duration earthquake loading history followed by a standard quasi-static cyclic loading protocol (see Figure 4).

[**]Specimen subjected to an initial dynamic pulse-type earthquake loading history followed by a standard quasi-static cyclic loading protocol (see Figure 4).

As shown in Figure 5a and b, irrespective of the type of initial EQ protocol (i.e. long duration or pulse-type), lower initial stiffness and residual displacement in the EQ-damaged specimens LD-1 and P-1, the force–displacement plots of both specimens were similar to that of specimen CYC once the EQ-damaged LD-1 and P-1 were pushed to drifts larger than 1.36%. Furthermore, the deformation capacities of CYC, LD-1, and P-1 were similar (see Table 1). The similarities in the force–displacement plots of specimens CYC, EQ-damaged LD-1, and P-1 at drift demands > 1.36% can be attributed to the fact that LSL was not initiated during the initial EQ protocol (i.e. the peak drift demand of 1.36% is less than the measured drift at LSL in specimen CYC – 1.9%).

These experimental observations also suggest that the hysteretic behavior of an EQ-damaged component would be similar to that of a pristine nominally identical component in a subsequent event at drift demands larger than the initial peak drift demand the EQ-damaged component was subjected to during the initial EQ.

On the other hand, LSL was reached during the initial EQ protocol in specimens LD-2 and P-2, resulting in reduced residual capacity—as observed by the lower residual strength and deformation capacity in EQ-damaged LD-2 and lower deformation capacity in EQ-damaged P-2 (see Table 1 and Figure 5c and d). The difference in the force-displacement response of EQ-damaged LD-2 and P-2 relative to specimen CYC is attributed to the fact that the initial EQ-protocol on pristine LD-2 and P-2 did not initiate LSL.

It is noteworthy that similar conclusions have been reached in a system-level study on two nominally identical frame structures subjected to different loading histories by Cecen (1979). Cecen (1979) concluded that two nominally identical EQ-damaged frames, subjected to different displacement histories, would have similar responses under a similar subsequent ground motion provided that the intensities of all the preceding displacement histories are not greater than that of the subsequent ground motion.

Results from tests on ductile beam specimens reported by Opabola and Elwood (2023) and Chiu et al. (2021) led to conclusions similar to those by Marder et al. (2018). For the sake of brevity, no detailed information of the experimental programs by Opabola and Elwood (2023) and Chiu et al. (2021) is provided here.
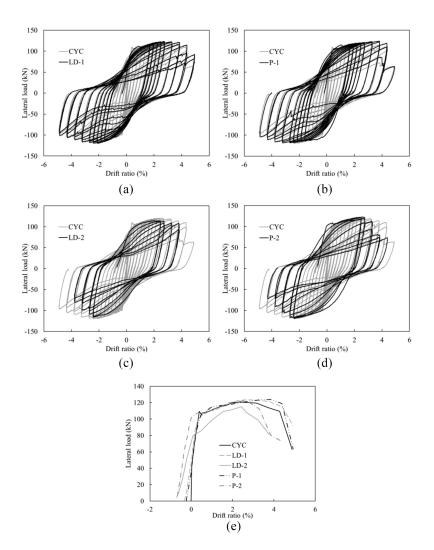
**Figure 5.** Force–displacement plots of beam specimens tested by Marder et al. (2018). (a) CYC vs EQ-damaged LD-1, (b) CYC vs EQ-damaged P-1, (c) CYC vs EQ-damaged LD-2, (d) CYC vs EQ-damaged P-2, (e) Backbones of all six specimens (LD-1, LD-2, P-1, and P-2 are EQ-damaged). EQ: earthquake.

Similar to frame members, experimental results from studies on the residual (reserve) capacity of RC walls are reviewed (i.e. tests involving the application of two sequential loading protocols). It is important to note that although the results reviewed herein are from tests on non-ductile (ordinary) flexure-controlled walls and shear-controlled walls, the concepts and conclusions are equally applicable to flexure-controlled walls.

Colmenares and Santa María (2021) conducted an experimental program on four flexure-controlled walls to understand the effect of number of cycles on the residual capacity of typical Chilean RC walls with unconfined boundaries. The baseline wall was tested under a standard cyclic loading protocol, while the other three walls were subjected to a cyclic loading protocol with a constant amplitude at a target drift of ~1.0% prior to
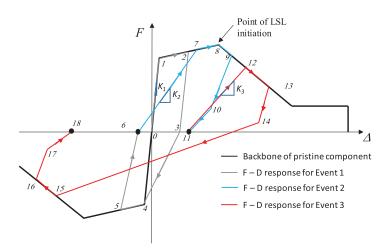
**Figure 6.** Peak-oriented reloading assumption.

applying the standard cyclic protocol. The varied parameter between the three tests was the number of cycles applied during the initial constant-amplitude protocol, which ranged from 30 to 120 cycles. Since the target drift was smaller than the drift capacity of the baseline wall at the initiation of LSL (roughly 2.0%), the number of cycles in the initial protocol did not have a noticeable effect on the strength and deformation capacity of the wall tests.

Furthermore, Moscoso et al. (2021) conducted an experimental study on walls with details similar to those tested by Colmenares and Santa María (2021), except that Moscoso et al. (2021) used a standard cyclic loading protocol for the initial loading. Wall RW2 S2.5 was tested initially under a standard cyclic loading protocol with maximum drifts of + 1.76% and –1.57%, which were close to drift capacity at the initiation of LSL of a companion specimen (RW1 S2.5) tested to failure under only a standard cyclic protocol. As a result, during the subsequent standard cyclic protocol, RW2 S2.5 was able to sustain only one additional cycle with a drift demand greater than the maximum drift reached during the initial protocol. However, for the other two wall tests (RW4 S2.5 and RW6 S1.75), since the maximum drift reached during the initial loading protocol was only about 50% of drift at the initiation of LSL, no noticeable effect on the strength and deformation capacity of the walls was observed.

The results above suggest that the behavior of an EQ-damaged component follows a "peak-oriented" assumption—that is, provided the drift at LSL of an EQ-damaged component was not reached in any preceding displacement histories (and no low-cycle fatigue issues), the residual capacity of the component is uncompromised.

Figure 6 is a graphical representation of the peak-oriented assumption using an arbitrary force-displacement plot for an arbitrary component that has been subjected to three arbitrary cyclic events, with each event imposing larger a peak deformation demand than the preceding one. Figure 6 shows that a damaged component will only be able to reach its original peak strength if the original component was subjected to initial cyclic demands lower than the drift capacity at the initiation of LSL (i.e. point 8). As shown in Figure 6, ductility demand histories reduce the effective stiffness (taken as the slope of the first force-displacement curve each event) of a damaged component (from $K_1$ to $K_2$ to $K_3$), irrespective of whether the drift at the initiation of LSL is reached or not.
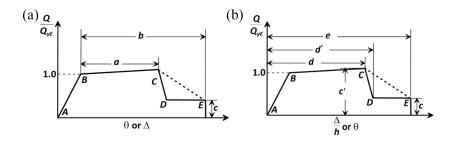
**Figure 7.** Idealized backbone relations given in ASCE/SEI 41-17 (2017) and ACI 369.1-23 (2023). (a) beam-column components and (b) walls.

## Proposed methodology for defining detailed visual inspection and repair limits

A key component of a post-EQ assessment procedure is the ability to identify locations for visual inspection (see Figure 1). In this procedure, the engineer would first develop an analytical model of the building and subject the model to ground motions recorded at or near the site. The demands on the components obtained from the analytical model are then compared with prescribed visual inspection limits to identify locations that may potentially have sustained damage. It is important that these detailed visual inspection limits are developed to have a low likelihood of missing damaged components during inspection, thereby warranting the need for these limits to be conservatively defined. In other words, it is better to inspect more locations than required, rather than inspecting fewer locations than necessary. As such, the detailed visual inspection limit is defined as the limit state beyond which some degree of component structural damage is expected, and thus visual inspection is necessary. The repair limit is defined as the limit state beyond which reduction in strength and deformation capacity of the component is expected, and thus significant (typically invasive) repair strategies are needed to restore the capacity of the structural components.

This section proposes a methodology for defining component deformation limits for visual inspection and repair for EQ-damaged concrete buildings.

### Defining deformation at the initiation of LSL ($\theta_{LSL}$)

As previously concluded, provided that the low-cycle fatigue limit state is not triggered, the influence of prior loading history on the residual capacity of ductile concrete components becomes significant only once the deformation at the initiation of LSL ($\theta_{LSL}$) is reached. State-of-practice standards for seismic evaluation and retrofit, such as ASCE/SEI 41, provide formulations or tables for evaluating component deformation capacities, typically at 20% LSL and at axial failure (AF). In this article, the deformation at 20% LSL is referred to as "lateral failure" or "LF." ASCE/SEI 41 provides component deformation capacities at LF in terms of either plastic hinge rotation (i.e. modeling parameter $a$) or total plastic hinge rotation (i.e. modeling parameter $d$) (see Figure 7 for the definition of these modeling parameters).

For structural walls, ASCE/SEI 41-17 (2017) nonlinear deformation-based modeling parameters are given as plastic hinge rotations (i.e. Parameters $a$ and $b$). However, approved updates of these provisions (Abdullah and Wallace, 2021b) for ACI 369.1-23
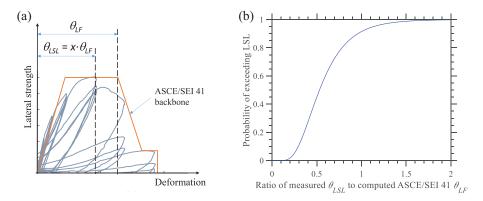
**Figure 8.** Definition of the ultimate component deformation limit (a) definition of deformation at LSL and (b) cumulative probability distribution of the ratio of measured $\theta_{LSL}$ to ASCE/SEI 41 deformation capacity at lateral failure ($\theta_{LF}$). LSL: lateral strength loss.

(2023) (which will be incorporated into the next ASCE/SEI 41) use total hinge rotation capacities for the deformation-based modeling parameters of flexure-controlled walls (Figure 7b), which include both the elastic and plastic deformations contributed by the hinge region (Abdullah, 2019). For this study, these updated modeling parameters are used for walls, as they represent the most accurate and up-to-date provisions and recommendations for flexure-controlled walls.

There are currently no codified formulations (in ASCE/SEI 41-17 (2017) or other documents) for predicting $\theta_{LSL}$ of concrete components. In this study, rather than developing new formulations for predicting $\theta_{LSL}$, it was considered more efficient to adopt a simple methodology of calibrating a multiplier, $x$, to be applied to the ASCE/SEI 41 deformation capacity at LF ($\theta_{LF}$) to obtain $\theta_{LSL}$ (see Figure 8a and Equation 1). If the ASCE/SEI 41 model for $\theta_{LF}$ is a reasonable estimate of mean deformation capacity at LF, then $x$ will be less than unity.

$$\theta_{LSL} = x \cdot \theta_{LF} \tag{1}$$

Using information from collated databases of experimental tests (described later) on concrete components (frame elements and walls), the statistical distribution (median and dispersion) of multiplier x can be evaluated by fitting a distribution to the calculated ratio of deformation capacity at LSL to deformation capacity at LF (see Figure 8b). The subsequent section describes the methodology proposed to develop the detailed visual inspection and repair limits, which are expressed as fractions of the ultimate component deformation limit.

### Defining the detailed inspection limit

In this section, a general methodology is proposed for defining the detailed visual inspection limits ($\theta_{IT}$) of structural components, which is defined such that there is a low likelihood that a location of damage will be missed. A reliability analysis, where all relevant sources of uncertainty are considered, is needed to accomplish this. For this study, a value of $p \leq 10\%$ is recommended based on engineering judgment. In addition to considering the uncertainty $\beta_{LSL}$ in predicting $\theta_{LSL}$ (see Figure 8b), uncertainties in demand estimates

**Table 2.** Distribution of key parameters in the frame component database

| Parameter | Statistical distribution | | | | | |
|---|---|---|---|---|---|---|
| | Beams | | | Columns | | |
| | Minimum | Average | Maximum | Minimum | Average | Maximum |
| Aspect ratio (a/d) | 1.7 | 3.1 | 4.8 | 2.3 | 4.4 | 7.5 |
| Longitudinal reinforcement ratio $\rho_L$ (%) | 1.1 | 1.9 | 3.4 | 1.2 | 2.6 | 6.0 |
| Transverse reinforcement ratio $\rho_t$ (%) | 0.2 | 0.75 | 1.6 | 0.35 | 1.0 | 3.0 |
| Spacing of transverse bars to effective depth (s/d) | 0.13 | 0.25 | 0.47 | 0.14 | 0.25 | 0.5 |
| Concrete compressive strength (MPa) [ksi] | 25 [3.6] | 58 [8.4] | 175 [25.4] | 23.6 [3.4] | 50 [7.25] | 115 [16.7] |
| Yield strength of longitudinal steel (MPa) | 280 [40.6] | 430 [62.4] | 585 [84.8] | 362 [52.5] | 444 [64.4] | 510 [74.0] |
| Axial load ratio $N/A_g f'_c$ | - | - | - | 0 | 0.25 | 0.5 |

from ground motion ($\beta_{gm}$) and modeling ($\beta_{model}$) need to be incorporated. The adopted approach in this study accounts for the fact that there could be a significant level of uncertainties in the demand estimates for various reasons, that is, the proximity of the structure to a ground motion recording station, availability and reliability of data obtained from building instrumentation, knowledgeability of material and structural properties, and complexity of adopted modeling techniques. For example, it is reasonable to assume that $\beta_{gm}$ and $\beta_{model}$ would be low for instrumented buildings and high for non-instrumented buildings. $\beta_{gm}$ would be low for a building with a ground motion station or a building situated near a ground motion station. The argument for $\beta_{model}$ follows the assumption that numerical models of instrumented buildings can be properly calibrated using data obtained from the instrumentation. From a post-EQ assessment perspective, $\beta_{model}$ could be further reduced if the engineer is able to improve their structural models using post-event observations on the expected behavior and failure modes of the components.

The authors are unaware of available studies with recommended values for $\beta_{gm}$ and $\beta_{model}$ for adoption in post-EQ probabilistic modeling and analysis. FEMA P-58 (FEMA, 2018) (in Table 5–2 of FEMA P-58) recommends values for $\beta_{model}$ depending on the quality and completeness of the analytical model, where $\beta_{model}$ values of 0.10, 0.25, and 0.40 are recommended for superior, average, and limited quality models. In this study, it is assumed that the $\beta_{model}$ for instrumented and non-instrumented buildings would be in the range of 0.10 to 0.40, respectively.

On the other hand, the record-to record variability values ($\beta_{RTR}$) provided in Table 5–3 of FEMA P-58 are deemed too conservative for adoption as $\beta_{gm}$ because it is expected that there would be a fair amount of available information from ground motion stations at or near the building, and the post-EQ assessment would likely not involve analyses using a suite of ground motion records. This study assumes that $\beta_{gm}$ ranges from zero for buildings with ground motion stations on-site to 0.70 for buildings without any ground motion stations on a similar site class within approximately 50 km (Abrahamson, 2021).

In this study, it is assumed that the random variables representing the deformation parameters (demand and capacity) are statistically independent and lognormally distributed. In

structural reliability terms, the limit state function for triggering the median $\tilde{\theta}_{LSL}$ can be written as Equation 2, where $\tilde{\theta}_D$ is the median component deformation demand:

$$G = \ln(\tilde{\theta}_{LSL}) - \ln(\tilde{\theta}_D) \tag{2}$$

The reliability index $Z$, accounting for the uncertainties in capacity and demand, can be computed as:

$$Z = \frac{\ln\left(\frac{\tilde{\theta}_{LSL}}{\tilde{\theta}_D}\right)}{\sqrt{\beta_{gm}^2 + \beta_{model}^2 + \beta_{LSL}^2}} \tag{3}$$

The reliability index $Z$ defines probability $p$ of $\tilde{\theta}_D$ exceeding $\tilde{\theta}_{LSL}$. The relationship between $Z$ and $p$ is defined as:

$$p = \Phi(-Z) \tag{4}$$

where $\Phi(.)$ is standard normal distribution function.

In this section, the limit state of interest is the detailed visual inspection limit, which is activated when $\tilde{\theta}_D \geqslant \theta_{IT}$. Replacing $\tilde{\theta}_D$ with $\theta_{IT}$ in Equation 3, $\theta_{IT}$ can be expressed as:

$$\theta_{IT} = \frac{\tilde{\theta}_{LSL}}{e^{Z\sqrt{\beta_{gm}^2 + \beta_{model}^2 + \beta_{LSL}^2}}} \tag{5}$$

where $1/e^{Z\sqrt{\beta_{gm}^2 + \beta_{model}^2 + \beta_{LSL}^2}}$ is the multiplier with respect to the median value of $\tilde{\theta}_{LSL}$ and defines the fraction of $\tilde{\theta}_{LSL}$ that $\theta_{IT}$ needs to be equal to, or to exceed, in order to trigger the limit state of interest. As previously stated, $\theta_{LSL}$ can be defined as a fraction of the deformation capacity at LF ($\theta_{LF}$), that is, $\theta_{LSL} = x \cdot \theta_{LF}$. Hence, $\theta_{IT}$ can also be expressed as:

$$\theta_{IT} = \frac{\tilde{\theta}_{LSL}}{e^{Z\sqrt{\beta_{gm}^2 + \beta_{model}^2 + \beta_{LSL}^2}}} = \frac{1}{e^{Z\sqrt{\beta_{gm}^2 + \beta_{model}^2 + \beta_{LSL}^2}}} \cdot \tilde{x} \cdot \tilde{\theta}_{LF} = x_{IT}\tilde{\theta}_{LF} \tag{6}$$

As such, the detailed visual inspection limit multiplier $x_{IT}$ is defined using the probability $p$ of exceeding $\theta_{LSL}$ (defined in terms of a reliability index $Z$), considering various sources of uncertainty. In Equation 6, $\beta_{LSL}$ and $x$ are the only parameters influencing $x_{IT}$ which are dependent on the component type.

## Defining the repair limit

The purpose of the component repair limit is to identify structural damage that needs safety-critical repair, which is defined as the deformation limit beyond which the lateral strength and deformation capacity of the component is compromised, and that safety-critical repair may be required to restore the structural characteristics of the component. A component below repair limit is still likely to see repairs for durability, aesthetics, and maybe serviceability.

In addition, the repair limit is used to fine-tune the analytical model of the building to accurately predict demands and damage, that is, to reconcile model results and observed damage. Therefore, the repair limit should not be as conservatively defined, as was the case for the detailed visual inspection limit, because the need for repair has to be confirmed through detailed visual inspection of the structural components by a professional engineer. For this study, the proposed repair limit is defined as the median estimate of $\theta_{LSL}$. As is demonstrated later using experimental data, the repair limit typically corresponds to the deformation at the initiation of longitudinal bar buckling in flexure-controlled components.

## Ductile frame components

### Description of database

As part of this study, a database of cyclic tests on ductile beams and columns was collated, where ductile components are defined as components where no brittle response was observed, ratio of transverse reinforcement spacing to effective depth ($s/d$) is not greater than 0.5, the shear capacity ratio (defined as the ratio of flexural strength to undegraded shear strength as defined by Sezen and Moehle, 2004) of the component is less than 0.6, and the transverse reinforcement is properly anchored with 135 degree hooks. This definition was adopted from ASCE/SEI 41-13 (2014). It is noted that all considered specimens were subjected to significant drift demands beyond peak strength. Furthermore, only test specimens with $N_{cyc}$ of 2 to 4 were considered.

The collated frame component database consists of 48 beams and 61 columns. The distribution of key parameters is presented in Table 2. Four of the beam specimens have concrete compressive strength greater than 100 MPa (14.5ksi). These four data points were not excluded from the database because it was of interest to extend the applicability of the framework over a wide range of steel and concrete properties.

For each component in the database, four drift capacities were extracted from the measured force-displacement backbones, as the drift at:

1. Yield (Y): estimated by drawing a secant line from the origin passing through the backbone curve of the first cycle at 70% of the maximum lateral load ($V_{max}$) and intersecting the horizontal line corresponding to $V_{max}$.
2. LSL: estimated as the drift at which the components start suffering LSL.
3. LF: defined as drift corresponding to $0.8V_{max}$.
4. AF: defined as the drift where the author(s) reported a loss of initial axial capacity or at which the lateral resistance has degraded to zero.

Furthermore, wherever reported, information on deformation demands at bar yielding, concrete cover spalling, longitudinal bar buckling, longitudinal bar fracture, and transverse bar fracture were collected. An example of a force-displacement curve with reported damage states is presented in Figure 9. It is noted that P-delta effects were consistently corrected for the backbones of the column specimens as described in Berry et al. (2004).

### Damage states of test specimens

The reported damage states from the frame component database were reviewed to identify the drift/rotation capacities at the initiation of LSL, which are used to propose detailed
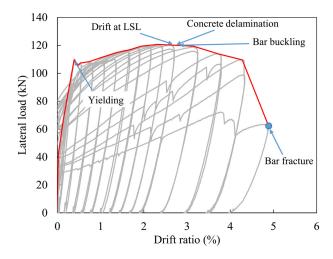
**Figure 9.** Example backbone curve and reported damage states for beam–column specimens in the collated database.
*Source.* Marder et al. (2018).

visual inspection and repair limits in the subsequent subsections. The typical damage sequence includes the formation of horizontal flexural cracks (in some components, diagonal-tension shear cracks are also observed), tensile yielding of longitudinal reinforcement, delamination and spalling of concrete in the extreme compression fiber, buckling of longitudinal reinforcement followed by fracture of longitudinal reinforcement with or without unhooking of transverse reinforcement.

It was of interest to identify the component damage state that influences the initiation of LSL in beam-column components. For the tests in the database, relevant information on drift corresponding to the reported observed damage were collected, which indicated that the drift at the initiation of LSL corresponds to the initiation of bar buckling (Figure 10). The ratio of measured drifts at the initiation of LSL to the drifts at the initiation of bar buckling has a mean of 1.0 (with a coefficient of variation of 0.10) for beams and a mean of 1.0 (with a coefficient of variation of 0.17) for columns. The high correlation between drift at the initiation of LSL and drift at bar buckling can be explained by the fact that bar buckling is associated with high localized strains, leading to high likelihood of fracture in subsequent cycles.

The observation that drift at the initiation of LSL corresponds to drift at the initiation of bar buckling further buttresses the choice of drift at the initiation of LSL as a threshold beyond which the component capacity is compromised. For components that experience bar buckling, it is expected that significant safety repair (typically in form of bar replacement) would be required to restore the component capacity. Prior to the initiation of bar buckling, only minor repair works related to concrete patching and epoxy injection may be required.

The authors note there may be significant uncertainty in accurately identifying the initiation of bar buckling (or kinking) by visual inspection, especially in cases where the concrete cover has not spalled yet. This was one of the main reasons this study decided to develop the proposed procedure around the deformation at LSL rather than bar buckling.
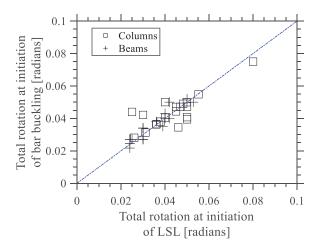
**Figure 10.** Comparison of measured drift at initiation of LSL to drift at the initiation of bar buckling for beams and columns. LSL: lateral strength loss.
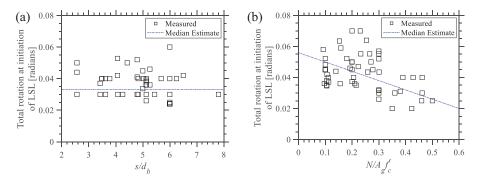


**Figure 11.** Total rotation at LSL for all beams and columns in the database (a) beams and (b) columns. LSL: lateral strength loss.

This approach also allowed this study to consider other test specimens where bar buckling information was not reported.

Figure 11 presents the variation of measured drift at the initiation of LSL against the ratio of transverse reinforcement spacing to bar diameter ($s/d_b$) for the beam tests and the axial load ratio ($N/A_g f'_c$) for the column tests. As shown in Figure 11b, there is a strong correlation between the drifts at the initiation of LSL and $N/A_g f'_c$.

## Defining the component deformation limit for ductile frame components

The lateral failure of beam-column components in ACI 369.1-23 is defined by modeling parameter $a$, which represents the plastic rotation capacity at 20% drop in lateral strength from peak strength. Following the methodology outlined above, this section seeks to define a multiplier $x$ that needs to be applied to ACI 369.1-23 modeling parameter $a$ for defining the component deformation limit corresponding to LSL ($\theta_{LSL}$) for beams and columns.
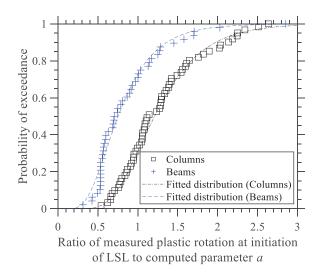
**Figure 12.** Cumulative distribution function for the ratio of measured plastic rotation at the initiation of LSL to computed modeling parameter *a*. LSL: lateral strength loss.

ACI 369.1-23 modeling parameter *a* for beams and columns are presented in Equations 7 and 8, respectively.

$$a = 0.042 - 0.043 \frac{N}{A_g f'_c} + 0.63\rho_t - 0.023 \frac{V_y}{V_o} \text{ for columns} \tag{7}$$

where $N$ is the axial load, $A_g$ is the gross cross-sectional area, $f'_c$ is concrete strength, $\rho_t$ is the transverse reinforcement ratio, $V_y$ is the flexural yield strength, and $V_o$ is the undegraded shear strength as provided in section 10.4.2.3.1 of ASCE/SEI 41-17.

$$a = 0.0055 \frac{M}{Vd} + 0.4\rho_t \frac{f_{yt}}{f'_c} - 0.008 \text{ for beams} \tag{8}$$

where $M/Vd$ is the shear span ratio, $f'_c$ is concrete strength, $\rho_t$ is the transverse reinforcement ratio, and $f_{yt}$ is the yield strength of the transverse reinforcement.

Following the outlined methodology, the ratio of plastic rotation at the initiation of LSL to the computed modeling parameter *a* was calculated for each beam–column component. Figure 12 represents the distribution of the ratio of plastic rotation at LSL to the computed a-value for beams and columns, respectively. For the beams, the median ratio equals 0.75*a* with a logarithmic distribution of 0.46. For the column specimens, the median ratio equals 1.2*a* with a logarithmic distribution of 0.38. The larger multiplier for the column specimens is attributed to the conservatism of modeling parameter *a* for ductile columns (See Ghannoum and Matamoros, 2014). It is noted that the ASCE/SEI 41-17 (2017) modeling parameter *a* model was fitted to a wide range of conforming and nonconforming column specimens with different failure modes (i.e. flexure, flexure-shear, and shear). This model achieves a median estimate across all column specimens in the database. However, this resulted in a bias for certain subset of columns (e.g. flexure-controlled columns with $s/d < 0.4$). For the entire column database, the median ratio of measured plastic rotation at the initiation of LSL to the measured plastic rotation at LF is 0.74 with a logarithmic dispersion of 0.3.

**Table 3.** Selecting a multiplier $x_{IT}$ to computed modeling parameter $a$ for assessing the detailed visual inspetion limit of ductile beams based on a 10% probability of exceedance (i.e. $Z = 1.28$)

| $\beta_{model}$ | $\beta_{gm}$ | | | | | | | |
|---|---|---|---|---|---|---|---|---|
| | 0.0 | 0.1 | 0.2 | 0.3 | 0.4 | 0.5 | 0.6 | 0.7 |
| 0.1 | 0.41 | 0.40 | 0.39 | 0.37 | 0.34 | 0.31 | 0.28 | 0.25 |
| 0.15 | 0.40 | 0.40 | 0.38 | 0.36 | 0.34 | 0.31 | 0.28 | 0.25 |
| 0.2 | 0.39 | 0.39 | 0.38 | 0.35 | 0.33 | 0.30 | 0.28 | 0.25 |
| 0.25 | 0.38 | 0.38 | 0.37 | 0.35 | 0.32 | 0.30 | 0.27 | 0.24 |
| 0.3 | 0.37 | 0.37 | 0.35 | 0.34 | 0.31 | 0.29 | 0.26 | 0.24 |
| 0.35 | 0.36 | 0.35 | 0.34 | 0.33 | 0.30 | 0.28 | 0.26 | 0.23 |
| 0.4 | 0.34 | 0.34 | 0.33 | 0.31 | 0.29 | 0.27 | 0.25 | 0.23 |
| Average | 0.40 0.32 | 0.40 | 0.38 | 0.36 | 0.34 | 0.31 | 0.28 | 0.25 |

**Table 4.** Selecting a multiplier $x_{IT}$ to computed $\theta_{LSL}$ for assessing the detailed visual inspection limit of ductile columns based on a 10% probability of exceedance (i.e. $Z = 1.28$)

| $\beta_{model}$ | $\beta_{gm}$ | | | | | | | |
|---|---|---|---|---|---|---|---|---|
| | 0.0 | 0.1 | 0.2 | 0.3 | 0.4 | 0.5 | 0.6 | 0.7 |
| 0.1 | 0.67 | 0.66 | 0.63 | 0.58 | 0.52 | 0.47 | 0.42 | 0.38 |
| 0.15 | 0.66 | 0.65 | 0.61 | 0.57 | 0.52 | 0.47 | 0.42 | 0.37 |
| 0.2 | 0.64 | 0.63 | 0.60 | 0.55 | 0.51 | 0.46 | 0.41 | 0.37 |
| 0.25 | 0.61 | 0.60 | 0.57 | 0.54 | 0.49 | 0.45 | 0.40 | 0.36 |
| 0.3 | 0.59 | 0.58 | 0.55 | 0.52 | 0.48 | 0.43 | 0.39 | 0.35 |
| 0.35 | 0.56 | 0.55 | 0.53 | 0.50 | 0.46 | 0.42 | 0.38 | 0.34 |
| 0.4 | 0.53 | 0.52 | 0.51 | 0.48 | 0.44 | 0.41 | 0.37 | 0.33 |
| Average | 0.61 0.5 | 0.60 | 0.57 | 0.53 | 0.49 | 0.44 | 0.40 | 0.36 |

To address the over-conservatism of the ASCE/SEI 41 formulation for ductile columns, a linear regression model was proposed to predict the drift at initiation of LSL for ductile columns (Equation 9). Equation 9 provides an estimate of the drift at initiation of LSL for ductile columns with a median ratio of 1.0 and logarithmic distribution of 0.29.

$$\theta_{LSL} = 0.056 - 0.06 \frac{N}{A_g f'_c} \leq 0.05 \text{ for columns} \tag{9}$$

Hence, if a future update to the ASCE/SEI 41 modeling parameter $a$ provides a good median estimate, the plastic rotation at the initiation of LSL can be updated to $0.74a$.

## Detailed visual inspection limits for ductile frame components

As previously mentioned, to avoid false negatives, the detailed visual inspection limit needs to be a lower-bound estimate with a high confidence level that there is a low probability of exceeding the component deformation limit at the initiation of LSL. Using the adopted methodology presented in this article, Tables 3 and 4 present the results of a parametric study, considering ground motion ($\beta_{gm}$), modeling ($\beta_{model}$) uncertainties, and values of unit-normal distribution parameter $Z$ (a function of probability $p\%$), to define a range of multipliers $x_{IT}$ to the computed a-values for the detailed visual inspection limit.

As shown in Table 3, adopting a $Z$-value of 1.28 (i.e. probability of exceeding $\theta_{LSL}$ p = 0.10) results in a multiplier to modeling parameter a with a range of 0.24 to 0.41 and an average value of 0.32 for ductile beams. Notably, the immediate occupancy (IO) limit in ASCE/SEI 41 is defined as 0.15a. Hence, depending on the considered modeling and ground motion uncertainties, the detailed visual inspection limit for ductile beams ranges from 1 to 2 times ASCE/SEI 41 IO limits.

As shown in Table 4 adopting a $Z$-value of 1.28 (i.e. probability of exceeding $\theta_{LSL}$ p = 0.10) results in a multiplier to modeling parameter a with a range of 0.4 to 0.7 and an average value of 0.54 for ductile columns. The detailed visual inspection limit for ductile columns ranges from 2 to 4.6 times ASCE-41 IO values.

### Repair limit for ductile frame components

The component deformation limits corresponding to the repair limit are proposed to correspond to the median estimate of the deformation at the initiation of LSL (i.e. initiation of bar buckling), which corresponds to a plastic rotation capacity of 0.75a for ductile beams and $1.0\theta_{LSL}$ for ductile columns.

## Ductile flexure-controlled walls

### Description of database

A comprehensive database (Abdullah, 2019; Abdullah and Wallace, 2019), which stores data on more than 1100 RC wall tests reported in the literature, was utilized to obtain a dataset of ductile (conforming) flexure-controlled walls. The reported information includes three major clusters of data: (1) information about the test specimen, test setup, and axial and lateral loading protocols; (2) computed data, for example, moment-curvature relationships and wall shear strength according to ACI 318-19 (2019); and (3) test results, for example, backbone relations and failure modes. Database information related to the objectives of this study are briefly presented below; however, detailed information about the database can be found elsewhere (Abdullah, 2019).

For buildings assigned to Seismic Design Category D, E, and F, design of RC structural walls is currently governed by the requirements of ASCE/SEI 7-16 (2016) and ACI 318-19 (2019), which includes provisions for structural walls with special boundary elements (SBE) that satisfy ACI 318-19 §18.10.6.4. Since the recommendations provided herein are applied for post-EQ assessment of buildings designed based on prior versions of ACI 318, as well as the current version, the database was filtered using the following criteria, some of which are less restrictive than the detailing requirements of ACI 318-19 §18.10.6.4 to cover walls with SBEs that are complaint to previous version of ACI 318 since 1983. It is noted that for simplicity, these walls are termed as ductile walls:

1. General criteria:

    (a) Flexure-controlled walls, that is, ratio of nominal shear strength to shear associated with nominal moment capacity, $V_n/V_{@Mn}$, > 1.0,
    (b) Walls with various cross-sections (planar, T-shaped, H-shaped, barbell-shaped, half barbell-shaped),
    (c) Walls tested under quasi-static, reversed cyclic loading,
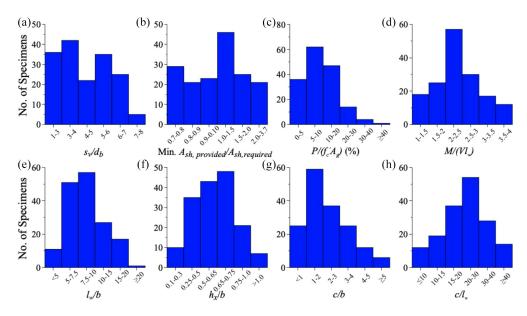
**Figure 13.** Histograms of the first dataset (188 tests) for walls with ductile detailing.

(d)   Walls with measured concrete compressive strength, $f'_c \geqslant 21$ MPa [3 ksi],

(e)   Walls with ratio of measured tensile-to-yield strength for boundary longitudinal reinforcement, $f_u/f_y \geqslant 1.2$, and

(f)   Walls with web thickness, $t_w, \geqslant 80$ mm [3.15 in.].

2.  Detailing criteria:

(a)   A minimum of two curtains of web vertical and horizontal reinforcement,

(b)   Ratio of provided-to-required (per ACI 318-19 Eq 18.10.6.4b) area of boundary transverse reinforcement, $A_{sh,provided}/A_{sh,required} \geqslant 0.7$,

(c)   Ratio of vertical spacing of boundary transverse reinforcement to minimum diameter of longitudinal boundary reinforcement, $s/d_b < 8.0$, and

(d)   Centerline distance between laterally supported boundary longitudinal bars, $h_x,$ between 25 mm [1.0 in.] and 240 mm [9.4 in.].

Based on the above-selected criteria, a total of 188 wall tests (hereafter referred to as ductile dataset) were identified. Histograms for various dataset parameters for the 188 tests are shown in Figure 13, where $P/A_g f'_c$ is the compressive axial load normalized by the measured concrete compressive strength ($f'_c$) and gross concrete area ($A_g$), and $M/Vl_w$ is the ratio of base moment-to-base shear normalized by wall length ($l_w$). Analysis of reported failure modes of about 1000 wall tests indicated that the flexure- and shear-controlled walls have a nominal shear-to-flexure strength ratio ($V_n/V_{@Mn}) > 1.0$ and $< 1.0$, respectively, whereas walls with failure modes reported as flexure-shear are mainly scattered between $0.7 < V_n/V_{@Mn} < 1.3$ (Abdullah, 2019). Walls with $t_w$ less than 88 mm [3.5 in.] were excluded because use of two curtains of web reinforcement along with realistic concrete cover is not practical in such thin walls. The limit on ratio $f_u/f_y$ is slightly less
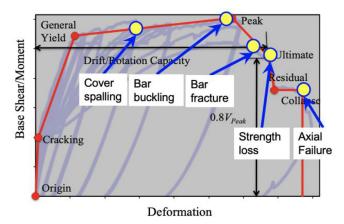
**Figure 14.** Example wall backbone curve contained in the wall database (Test by Tran and Wallace, 2015).

restrictive than the limit of 1.25 specified in ACI 318-19 §20.2.2.5. The specified limits on $s/d_b \leqslant 8.0$ and $A_{sh, provided}/A_{sh, required}$ ($A_{sh}$ required by ACI 318-19 Eq 18.10.6.4b) $\geqslant 0.7$ are slightly less restrictive than the current limits in ACI 318-19 §18.10.6.4 of 6.0 and 1.0, respectively. Finally, the cyclic loading protocols used for these 62 walls consisted for either one repeated cycle (1 wall), two repeated cycles (23 walls) or three repeated cycles (38 walls) at each load/deformation demand.

It is noted this dataset is the same dataset used by the authors to develop the updated modeling parameters and acceptance criteria for ACI 369-1.23 (see Abdullah, 2019).

The database includes reported failure mode and backbone relations (e.g. base shear-total top displacement), consisting of seven points (origin, cracking, general yielding, peak, ultimate, residual, and axial failure), as shown in Figure 14. In addition, the database includes reported deformation at key damage states such as initiation of concrete cover spalling, initiation longitudinal bar buckling, and longitudinal bar fracture, if such information is reported in the reference document. Out of the 188 wall tests in the ductile dataset, 62 walls had at least reported deformation corresponding to initiations of cover spalling and bar buckling. This smaller subset (62 walls) was utilized for the recommendations proposed herein, especially identifying hinge deformation capacity at initiation of LSL ($\theta_{LSL}$). It is noted that only half of the walls in this subset had reported bar fracture because this information was either not reported or the wall did not experience longitudinal bar fracture and failed due to out-of-plane instability or, in a rare case, due to crushing of concrete in the web region next to the boundary elements (common in barbell or flanged walls). The statistics (medians and lognormal standard deviations) and fragility curves for total hinge rotation capacities at each key damage state normalized by $d$ from ACI 369-1.23 are presented in Table 5 and Figure 15, respectively.

## Damage states and deformation at initiation of LSL

In this subsection, results and damage states typical of ductile flexure-controlled walls are reviewed to identify the hinge rotation capacity at initiation of LSL, which is used to propose detailed visual inspection and repair limits later. For ductile flexure-controlled walls subjected to gradual increase of cyclic demands, the damage sequence typically involves:

**Table 5.** Statistics for rotation at key damage states of ductile flexure-controlled walls as fractions of Parameter *d*

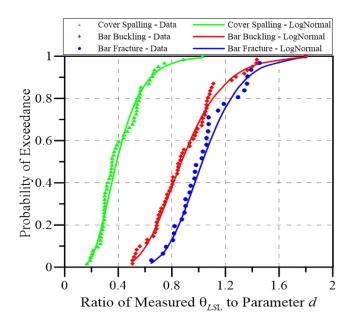| Damage state | Mean | Median | LogNormal standard deviation |
|---|---|---|---|
| Cover spalling | 0.42 | 0.35 | 0.39 |
| Bar buckling | 0.91 | 0.86 | 0.28 |
| Bar fracture | 1.05 | 1.02 | 0.22 |



**Figure 15.** Fragility curves for key damage states of the ductile wall dataset.

(a) Formation of horizontal cracks initiating from the extreme edges of the wall with or without diagonal (tension) shear cracks in the web,

(b) Sequential yielding of longitudinal bars till the effective yield strength is reached,

(c) Spalling of concrete cover at the extreme fibers of the wall (boundary elements),

(d) Buckling of extreme longitudinal bars in the boundaries, resulting in initiation of LSL (e.g. Figure 16),

(e) Fracture of buckled bars combined with concrete core crushing, opening or fracture of hoops and crossties, or local instability, leading to significant loss of lateral strength ($\geq$ 20%). In walls with shear stress exceeding $0.5\sqrt{f'_c}\,(in\ MPa)$ [$6\sqrt{f'_c}\,(in\ psi)$], loss of lateral strength is likely due to crushing of the web region adjacent to the boundary elements,

(f) Gradual loss of lateral strength as a result of sequential fracture of longitudinal bars and concrete crushing for walls with low compression demands (depth of neutral axial/width of flexural compression zone, $c/b$, $< 2$) and squat cross-sections ($l_w/b- \leq 10$), or crushing of concrete or out-of-plane instability across the entire length of the wall for walls with significant compression demands and slender cross-sections ($c/b$, $> 4$ and $l_w/b > 15$), leading to abrupt loss of axial load-carrying capacity.
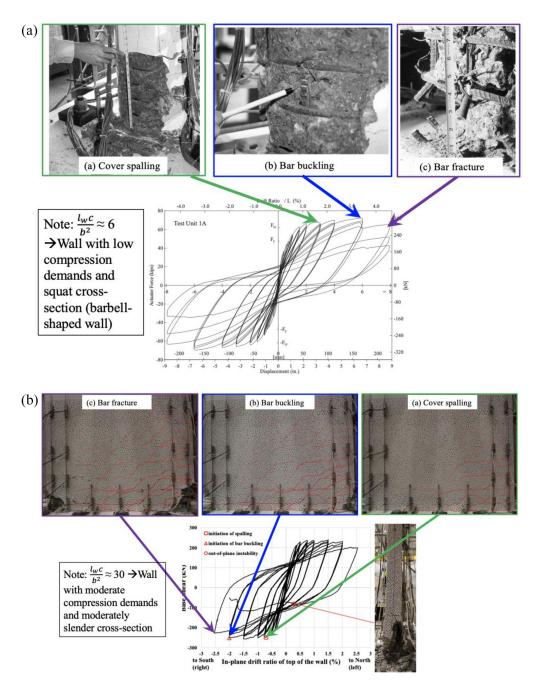
**Figure 16.** Examples of damage states of ductile flexure-controlled walls (a) Hines et al. (2002) and (b) Niroomandi et al. (2018).

Review of damage states of walls in the dataset (e.g. as shown in Figure 16) suggested that initiation of LSL of ductile flexure-controlled walls is typically associated with buckling of longitudinal bars in the boundary elements. Once longitudinal bars buckle, the concrete core loses part of the confining pressure and begins to crush, and, as a result, the
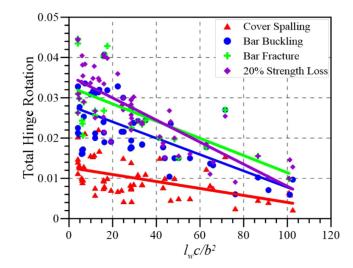
**Figure 17.** Comparison of hinge rotation capacity of the dataset at key damage states.

depth of neutral axis shifts inward, leading to a smaller moment arm and thus reduction in moment capacity. Thus, longitudinal bar buckling is considered as the damage state beyond which the residual capacity of the wall (in terms of strength and deformation capacity) is compromised, and that structural repair might be needed to restore its structural characteristic for future events.

Figure 17 compares the hinge rotation capacities of the reduced dataset of 62 wall tests at the three key damage states and indicates that the rotation capacities for all three damage states vary significantly (by a factor of 2.0–4.0), although all the walls are fully or nearly code-compliant. In addition, there is a significant buffer zone (on average about 0.01 hinge rotation) between occurrence of initiation of cover spalling and initiation of bar buckling, indicating that it is unlikely for cover spalling and bar buckling damage states to happen simultaneously in a ductile wall. As was shown in Table 5, the median values of rotation at cover spalling and bar buckling normalized by Parameter $d$ are 0.35 and 0.86, respectively, indicating that median values of hinge rotation capacity at bar buckling are more than twice the rotation capacity at cover spalling. This suggests that the use of cover spalling as the component deformation limit for repair might be overly conservative. Figure 17 and Table 5 also indicate that there is only a slight reserve rotation capacity between bar buckling and bar fracture (median value of ratios of rotation at bar buckling to bar fracture $\approx 0.86$), and that fracture of the extreme layer of longitudinal bars results in roughly 20% LSL, which is typically defined as LF (median value of ratios of rotation at bar fracture to LF $\approx 1.0$). These results support the approach of using the damage state of longitudinal bar buckling as the component deformation limit for ductile flexure-controlled walls.

Finally, Figure 17 indicates that there is a significant correlation between hinge rotation capacity and a slenderness parameter, $(l_w/b)(c/b) = l_w c/b^2$, where $l_w$ is the length of the wall, $c$ is the depth of neutral axial corresponding to a concrete compressive strain of 0.003, and $b$ is the width of the flexural compression zone. This parameter provides an efficient means to account for the slenderness of the cross-section $(l_w/b)$ and the slenderness of the flexural compression zone of the cross-section $(c/b)$ on the deformation capacity of

**Table 6.** Multipliers $x_{IT}$ for assessing the detailed visual inspection limit of ductile walls based on a 10% probability of exceedance (i.e. $Z = 1.28$)

| $\beta_{model}$ | $\beta_{gm}$ | | | | | | | |
|---|---|---|---|---|---|---|---|---|
| | 0.0 | 0.1 | 0.2 | 0.3 | 0.4 | 0.5 | 0.6 | 0.7 |
| 0.00 | 0.60 | 0.59 | 0.55 | 0.51 | 0.46 | 0.41 | 0.37 | 0.33 |
| 0.05 | 0.60 | 0.58 | 0.55 | 0.51 | 0.46 | 0.41 | 0.37 | 0.33 |
| 0.10 | 0.59 | 0.58 | 0.54 | 0.50 | 0.45 | 0.41 | 0.36 | 0.32 |
| 0.15 | 0.57 | 0.56 | 0.53 | 0.49 | 0.45 | 0.40 | 0.36 | 0.32 |
| 0.20 | 0.55 | 0.54 | 0.52 | 0.48 | 0.44 | 0.40 | 0.35 | 0.32 |
| 0.25 | 0.53 | 0.52 | 0.50 | 0.46 | 0.43 | 0.39 | 0.35 | 0.31 |
| 0.30 | 0.51 | 0.50 | 0.48 | 0.45 | 0.41 | 0.38 | 0.34 | 0.30 |
| 0.35 | 0.48 | 0.48 | 0.46 | 0.43 | 0.40 | 0.36 | 0.33 | 0.30 |
| 0.40 | 0.46 | 0.45 | 0.44 | 0.41 | 0.38 | 0.35 | 0.32 | 0.29 |
| Average | 0.54 0.44 | 0.53 | 0.51 | 0.47 | 0.43 | 0.39 | 0.35 | 0.31 |

ductile flexure-controlled walls (Abdullah and Wallace, 2019). Walls with values of $l_w c/b^2$ lower than 10 tend to be flexure-tension controlled and generally have large deformation capacities (e.g. Figure 16), whereas walls with values of $l_w c/b^2$ exceeding 70 (slender cross-sections and large compression zones) tend to be flexure-compression-controlled and generally have low deformation capacities and simultaneous occurrence of lateral and axial failures (Abdullah and Wallace, 2021a), suggesting that these walls could be considered as components always requiring inspection. Further review of the data revealed that rotation capacity at the initiation of bar buckling is moderately impacted by the longitudinal bar slenderness ratio, $s/d_b$, which ranges from 2.5 to 8.0 in the reduced dataset.

### Detailed visual inspection limits for ductile walls

As discussed previously, the purpose of the component deformation limit for detailed visual inspection limit state is to help the engineer identify locations that may have potentially sustained structural damage for visual inspection. Using the proposed methodology described previously and the uncertainty in the capacity reported in Table 5, a parametric study was carried out to determine the range of multipliers on Parameter $d$ for component deformation limits for inspection of ductile flexure-controlled walls. The results are presented in Table 6, which indicates that, depending on the variability associated with modeling and the ground motion, the multipliers range from 0.29 to 0.6, with average values of 0.44. Figure 15 indicates that a detailed visual inspection limit of $0.4d$ roughly corresponds to a median value of rotation at cover spalling, which confirms the rationale of the approach used to select the detailed visual inspection limit. That is, when there is 50% probability that cover spalling has occurred, visual inspection should be conducted to confirm whether the element has sustained structural damage in the form of bar buckling and/or fracture.

In the updated nonlinear acceptance criteria for flexure-controlled walls in ACI 369-1.23, IO performance objective is defined as the sum of elastic hinge rotation and 10% of the inelastic hinge rotation, that is, $IO = \theta_y + 0.1(d - \theta_y)$. For ductile flexure-controlled walls, $\theta_y$ typically ranges from 0.3% to 0.4%. Assuming $\theta_y \approx 0.35\%$, $IO \approx 0.4\%$ to 0.64% rotation and $\approx 0.2$ to $0.4\ d$. Thus, detailed visual inspection limit of $0.4d$ is roughly 1 to 2 times IO, as can be seen in Figure 18.
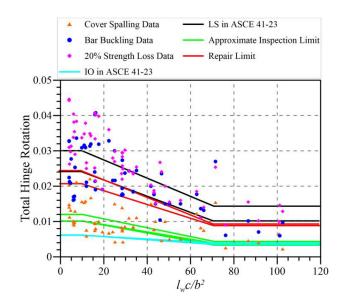
**Figure 18.** Comparison of proposed component deformation limits for detailed visual inspection and repair with experimental data and performance objectives in ACI 369-1.23.
*Note.* Same lines show the range of the parameter.

It should be recognized that there are vertical load-carrying components whose probable residual capacity may not be reliably assessed, or their post-LSL behavior is relatively brittle, that is, once the lateral strength degradation initiates, the component possesses little or no additional deformation capacity before axial failure occurs (Abdullah and Wallace, 2019, 2021a); and thus failure of such components in a subsequent event may result in catastrophic consequences. It is recommended that such components be inspected regardless of whether the inspection trigger is exceeded or not. Also, careful engineering judgment should be exercised when classifying such components as those not requiring repair. Examples of walls described in this study and are falling in this category include flexure-controlled walls with values of $l_w c / b^2$ exceeding 70.

### Repair limit for ductile walls

As discussed previously, this limit is defined as the median value of hinge rotation capacity at bar buckling, that is, 50% probability of reaching initiation of LSL. Table 5 shows that the median value of hinge rotation capacity at bar buckling corresponds to a repair limit of $0.86d$. To account for the possibility of bar buckling occurring prior to the reported observation (i.e. buckled bars being concealed by split but un-spalled concrete cover), a slightly smaller multiplier for repair limit, that is, $0.8\,d$, is proposed. Figure 15 shows that median value of rotation at bar buckling corresponds to roughly 25% probability of bars fracturing and almost 100% probability of cover spalling.

The LS performance objective in ACI 369-1.23 is defined as 0.75 Parameter *e* (rotation at AF), which is roughly equal to $0.9\,d$, resulting in the repair limit ($0.8\,d$) being equal to about 0.9 times LS. Figure 18 compares the proposed repair limit with the hinge rotation capacity data of the reduced dataset and LS performance objective. Recommended component deformation limits.

**Table 7.** Adopted lognormal dispersions for defining detailed visual inspection limits

| Uncertainty source | Instrumented building | Distance to closest ground motion station on the same site class | | |
|---|---|---|---|---|
| | | 0 km (instrument on site) | 5 km | No instrument within 20 km |
| $\beta_{gm}$ | 0.0 | 0.0 | 0.4 | 0.6 |
| $\beta_{model}$ | 0.1 | 0.2 | 0.2 | 0.2 |

**Table 8.** Proposed deformation limits for visual inspection and structural repair

| Components | Component deformation limits | | | | |
|---|---|---|---|---|---|
| | Visual Inspection | | | | Repair |
| | Instrumented building | Distance to the nearest ground motion station on the same site class | | | |
| | | 0 km | 5 km | > 20 km | |
| Beams | $0.39a^{*}$ | $0.37a$ | $0.31a$ | $0.26a$ | $0.75a$ |
| Columns[**] | $0.67\theta_{LSL}$ | $0.64\theta_{LSL}$ | $0.51\theta_{LSL}$ | $0.41\theta_{LSL}$ | $1.0\theta_{LSL}$ |
| Walls | $0.59d^{*}$ | $0.56d$ | $0.44d$ | $0.36d$ | $0.8d$ |

LSL: lateral strength loss.
[*]As defined in ACI 369.1-23.
[**]As defined in Equation 9.

As earlier mentioned, visual inspection limits are needed to identify locations requiring detailed inspection. For defining these limits, recommended lognormal dispersions in the demand (i.e. ground motion, $\beta_{gm}$, and modeling, $\beta_{model}$) are presented Table 7, where $\beta_{gm}$ is defined as a function of the building distance to the closest ground motion station on the same site class. This study assumes $\beta_{gm}$ = zero for instrumented buildings and buildings with a ground motion station on site. It is noteworthy that $\beta_{gm}$ has been defined to account for within-event spatial correlation in ground shaking. Furthermore, $\beta_{model}$ is taken as 0.1 and 0.2 for instrumented and non-instrumented buildings. Based on these dispersions, component deformation limits for visual inspection are selected from Tables 3, 4, and 6, and presented in Table 8. Furthermore, Table 8 presents the component deformation limits for safety-critical repair, which are defined to correspond to the median estimate of the deformation at the initiation of LSL, as noted previously.

## Conclusions and recommendations

This study examines experimental data on ductile flexure-controlled RC beams, columns, and walls to understand the impact of prior displacement history on the residual capacity of these components. Based on the findings, the following conclusions and recommendations are given:

1. Provided that the deformation at initiation of LSL of an RC component is not exceeded in any previous loading histories (prior EQs) and low-cycle fatigue is not triggered, aside from a reduction in initial stiffness, the residual (reserve) capacity (in terms of strength and deformation capacity) of the EQ-damaged component is likely uncompromised.

2. Damage progression data suggest that the initiation of LSL corresponds to the onset of bar buckling for flexure-controlled components. It was also concluded that the deformation at LSL (longitudinal bar buckling) equals 0.75 and 1.2 times ACI 369-1.23 modeling parameter *a* for ductile beams and columns respectively, and 0.8 times ACI 369-1.23 modeling parameter *d* for ductile structural walls. Thus, these component deformation limits are recommended to be adopted as structural repair limits for these components.

3. A general framework for defining component deformation limits triggering a detailed visual inspection, which are also expressed as fractions of ASCE/SEI 41 modeling parameters at LF, is proposed. These limits are defined such that there is a low probability ($\leqslant 10\%$) of exceeding the deformation at the initiation of LSL, considering relevant sources of uncertainty in demand (modeling and ground motion) and capacity (deformation at LSL). Based on this, an array of detailed visual inspection limits are proposed for each component for various combinations of said uncertainties.

## ORCID iD

Eyitayo A Opabola  https://orcid.org/0000-0002-7598-4812

## References

Abdullah SA (2019) *Reinforced concrete structural walls: Test database and modeling parameters.* PhD Dissertation, Department of Civil and Environmental Engineering, University of California, Los Angeles, Los Angeles, CA.

Abdullah SA and Wallace JW (2019) Drift capacity of RC structural walls with special boundary elements. *ACI Structural Journal* 116(1): 183–194.

Abdullah SA and Wallace JW (2021a) Drift capacity at axial failure of RC structural walls and wall piers. *Journal of Structural Engineering: ASCE* 147(6): 04021062.

Abdullah SA and Wallace JW (2021b) Nonlinear modeling parameters and acceptance criteria for RC structural walls. In: *Proceedings of the 2021 Los Angeles tall buildings structural design council conference*, Los Angeles, CA, 12 November.

Abdullah SA, Aswegan K, Klemencic R and Wallace JW (2020) *Experimental study of concrete coupling beams subjected to wind and seismic loading protocols.* Report no. UCLA SEERL 2020/01 (Submitted to Magnusson Klemencic Associates Foundation), May 2020, p. 268. Los Angeles, CA: *University of California, Los Angeles.*

Abrahamson N (2021) Personal communication (Email) with Jack Moehle, 2 September 2021.

American Concrete Institute (ACI) 318-19 (2019) *Building Code Requirements for Structural Concrete* (ACI Committee 318). Farmington Hills, MI: ACI.

American Concrete Institute (ACI) 369.1-23 (2023) *Standard Requirements for Seismic Evaluation and Retrofit of Existing Concrete Buildings* (ACI Committee 369). Farmington Hills, MI: ACI.

American Society of Civil Engineers (ASCE)/SEI 7-16 (2016) *Minimum Design Loads and Associated Criteria for Buildings and Other Structures.* Reston, VA: ASCE.

American Society of Civil Engineers (ASCE)/SEI 41-13 (2014) *Seismic Evaluation and Retrofit of Existing Buildings.* Reston, VA: ASCE.

American Society of Civil Engineers (ASCE)/SEI 41-17 (2017) *Seismic Evaluation and Retrofit of Existing Buildings.* Reston, VA: ASCE.

Berry M, Parrish M and Eberhard M (2004) *PEER Structural Performance Database User's Manual* (version 1.0). Berkeley, CA: Pacific Earthquake Engineering Research Center (PEER), University of California, Berkeley, 38 pp.

Cecen H. (1979) Response of ten story, reinforced concrete model frames to simulated earthquakes. PhD thesis, *University of Illinois at Urbana-Champaign.*

Chiu, C. K., Sung, H. F., and Chiou, T. C. (2021) Quantification of the reduction factors of seismic capacity for damaged RC column members using the experiment database. *Earthquake Engineering & Structural Dynamics*, 50(3): 756–776.

Colmenares J and Santa María H (2021) Effect of number of cycles on the residual capacity of RC structural walls with unconfined boundaries. *Presentation at 2nd virtual workshop on residual capacity*. February 17, 2021.

Di Ludovico M, Polese M, Gaetani d'Aragona M, Prota A and Manfredi G (2013) A proposal for plastic hinges modification factors for damaged RC columns. *Engineering Structures* 51: 99–112.

Elwood KJ, Sarrafzadeh M, Pujol S, Liel A, Murray P, Shah P and Brooke NJ (2021) Impact of prior shaking on earthquake response and repair requirements for structures —Studies from ATC-145. In: *Proceedings of the 2021 NZSEE conference*, Christchurch, New Zealand, 14–16 April.

Federal Emergency Management Agency (FEMA) (1998a) *FEMA 306: Evaluation of Earthquake Damaged Concrete and Masonry Wall Buildings: Basic Procedures Manual.* Washington, DC: FEMA.

Federal Emergency Management Agency (FEMA) (1998b) *FEMA 307: Evaluation of Earthquake Damaged Concrete and Masonry Wall Buildings—Technical Resources.* Washington, DC: FEMA.

Federal Emergency Management Agency (FEMA) (2018) *Seismic Performance Assessment of Buildings Guidelines (FEMA P—58) Volume 1—Methodology.* 2nd ed. Washington, DC: FEMA.

Ghannoum WM and Matamoros AB (2014) Nonlinear modeling parameters and acceptance criteria for concrete columns. *ACI Structural Journal* 297: 1–24.

Hines EM, Seible F and Priestley MJN (2002) Seismic performance of hollow rectangular reinforced concrete piers with highly-confined corner elements -Phase I: Flexural tests, and Phase II: Shear tests. *Structural Systems Research Project (SSRP)-99/15*, February 2002, 266 pp. San Diego, CA: University of California, San Diego.

Kawashima K and Koyama T (1988) Effect of number of loading cycles on dynamic characteristics of reinforced concrete bridge pier columns. *Structural Engineering/Earthquake Engineering* 5(1): 205–213.

Maeda M, Koike T, Hosoya N, Suzuki Y, Tsurugai K and Nimura A (2017) Damage and residual seismic performance evaluation of reinforced concreate shear walls. In: *Proceedings of the 16th world conference on earthquake*, Santiago, 9–13 January.

Marder K (2018) *Post-earthquake residual capacity of reinforced concrete plastic hinges*. PhD Thesis, The University of Auckland, Auckland, New Zealand.

Marder K, Motter C, Elwood KJ and Clifton GC (2018) Testing of 17 identical ductile reinforced concrete beams with various loading protocols and boundary conditions. *Earthquake Spectra* 34(3): 1025–1049.

Marquis F, Kim JJ, Elwood KJ and Chang SE (2017) Understanding post-earthquake decisions on multi-storey concrete buildings in Christchurch, New Zealand. *Bulletin of Earthquake Engineering* 15: 731–758.

Moscoso JF, Hube MA and Santa María H (2021) Residual seismic capacity of reinforced concrete walls with unconfined boundaries. *ACI Structural Journal* 118(5): 205–220.

Niroomandi A, Pampanin S, Dhakal RP, Soleymani Ashtiani M and De La Torre C (2018) Rectangular RC walls under bi-directional loading: Recent experimental and numerical findings. In: *Proceedings of the New Zealand concrete industry conference*, Hamilton, New Zealand, 11–13 October.

Oesterle, R. G., Aristizabal-Ochoa, J. D., Fiorato, A. E., Russell H. G., and Corley, W. G (1979) "Earthquake Resistant Structural Walls–Phase II", Report to National Science Foundation (ENV77-15333), Construction Technology Laboratories. *Portland Cement Association*, October, 1979, Skokie, IL, 331 pp.

Opabola EA and Elwood KJ (2023) Seismic performance of reinforced concrete beams susceptible to single-crack plastic hinge behavior. *Journal of Structural Engineering: ASCE*. Epub ahead of print 8 February. DOI: 10.1061/JSENDH.STENG-11424.

Sezen H and Moehle JP (2004) Shear strength model for lightly reinforced concrete columns. *Journal of Structural Engineering: ASCE* 130(11): 1692–1703.

Tran TA and Wallace JW (2015) Cyclic testing of moderate-aspect-ratio reinforced concrete structural walls. *ACI Structural Journal* 112(6): 653–666.